MODELLING THE LIGHT FIELD IN MACROALGAE AQUACULTURE

A Thesis

Presented to

The Graduate Faculty of The University of Akron

In Partial Fulfillment

of the Requirements for the Degree

Master of Science

Oliver Graham Evans

May, 2018

MODELLING THE LIGHT FIELD IN MACROALGAE AQUACULTURE

Oliver Graham Evans

Thesis

Approved: Accepted:

_____   _____
Advisor   Dean of the College
Dr. Kevin Kreider   Dr. John Green

_____   _____
Co-Advisor   Dean of the Graduate School
Dr. Curtis Clemons   Dr. Chand Midha

_____   _____
Faculty Reader   Date
Dr. Gerald Young

_____
Department Chair
Dr. Kevin Kreider

ABSTRACT

A probabilistic model for the spatial distribution of kelp fronds is developed based on a kite-shaped geometry and simple assumptions about the motion of fronds due to water velocity. Radiative transfer theory is then applied to determine the radiation field by using the kelp model to determine optical properties of the medium. Finite difference and asymptotic solutions are explored, and behavior of the results over the parameter space is investigated. Numerical simulations to predict the lifetime biomass production of kelp plants are performed to compare our light model to the previous exponential decay model.

ACKNOWLEDGEMENTS

TABLE OF CONTENTS

LIST OF TABLES

LIST OF FIGURES

CHAPTER I

INTRODUCTION

1.1   Motivation

Given the global rise in population, efficient and innovative resource utilization is increasingly important. Future generations face major challenges regarding food, energy, and water security while addressing major issues associated with global climate change. Growing concern for the negative environmental impacts of petroleum-based fuel is generating a market for biofuel, especially corn-based ethanol. However, corn-based ethanol has been heavily criticized for diverting land usage away from food production, for increasing use of fertilizers that impair water quality, and for low return on energy investments for production. At the same time, a great deal of unutilized saltwater coastline is available for both food and fuel production through seaweed cultivation. Specifically, the sugar kelp *Saccharina latissima* is known to be a viable source of food, both for direct human consumption and biofuel production.

Nitrogen leakage into water bodies is a significant ecological problem, and is especially relevant near large conventional agriculture facilities due to run-off from nitrogen-based fertilizers, as well as near wastewater treatment plants. Waste water treatment plants (WWTPs) in particular are facing increasingly stringent regula-

1

tion of nutrients in their effluent discharges from the US Environmental Protection Agency (USEPA) and state regulatory agencies. Nutrient management at WWTPs requires significant infrastructure, operations, and maintenance investments for tertiary treatment processes. Many treatment works are constrained financially or by space limitations in their ability to expand their treatment works. As an alternative to conventional nutrient remediation techniques, the cultivation of the macroalgae *Saccharina latissima* (sugar kelp) within the nutrient plume of WWTP ocean outfalls has been proposed. The purpose of such an undertaking would be twofold: to prevent eutrophication of the surrounding ecosystem by sequestering nutrients, and to provide supplemental nutrients that benefit macroalgae cultivation.

Large scale macroalgae cultivation has long existed in Eastern Asia due to the popularity of seaweed in Asian cuisine, and low labor costs that facilitate its manual seeding and harvest. More recently, less labor-intense and more industrialized kelp aquaculture has been developing in Scandinavia and in the Northeastern United States and Canada. For example, the MACROSEA project is a four year international research collaboration led by SINTEF, an independent research organization in Norway, and funded by the Research Council of Norway targeting "successful and predictable production of high quality biomass thereby making significant steps towards industrial macroalgae cultivation in Norway." The project includes both cultivators and scientists, working to develop a precise understanding of the full life cycle of kelp and its interaction with its environment. A fundamental aspect of this endeavor is the development of mathematical models to describe the growth of kelp.

Recently, a growth model [2] for S. latissima has been produced and integrated into the SINMOD [14] hydrodynamic and ecosystem model of SINTEF. One aspect of the model which has yet to be fully developed is the availability of light, considering factors such as absorption and scattering by the aquatic medium, as well as by the kelp itself. This thesis contributes to this effort by developing a first-principles model of the light field in a kelp farming environment. As a first step, a model for the spatial distribution of kelp is developed. Radiative transfer theory is then applied to determine the effects of the kelp and water on the availability of light throughout the medium. A numerical finite difference solution to the Radiative Transfer Equation, followed by asymptotic approximations that prove to be sufficiently accurate and less computationally intensive. A detailed description of the numerical solution of this model, accompanied by source code for a FORTRAN implementation of the solution. This model can be used independently, or in conjunction with a kelp growth model to determine the amount of light available for photosynthesis at a single time step.

1.2   Background on Kelp Models

Mathematical modeling of macroalgae growth is not a new topic, although it is a reemerging one. Several authors in the second half of the twentieth century were interested in describing the growth and composition of the macroalgae *Macrocystis pyrifera*, commonly known as "giant kelp," which grows prolifically off the coast of southern California. The first such mathematical model was developed by W.J. North for the Kelp Habitat Improvement Project at the California Institute of Technology

3

Figure 1.1: *Saccharina latissima* being harvested

in 1968 using seven variables. By 1974, Nick Anderson greatly expanded on North's work, and created the first comprehensive model of kelp growth which he programmed using FORTRAN [1]. In his model, he accounts for solar radiation intensity as a function of time of year and time of day, and refraction on the surface of the water. He uses a simple model for shading, simply specifying a single parameter which determines the percentage of light that is allowed to pass through the kelp canopy floating on the surface of the water. He also accounts for attenuation due to turbidity using Beer's Law. Using this data on the availability of light, he calculates the photosynthesis rates and the growth experienced by the kelp.

Over a decade later in 1987, G.A. Jackson expanded on Anderson's model for *Macrocystis pyrifera*, with an emphasis on including more environmental parameters and a more complete description of the growth and decay of the kelp [7]. The author takes into account respiration, frond decay, and sub-canopy light attenuation due to self-shading. Light attenuation is represented with a simple exponential model, and self-shading appears as an added term in the decay coefficient. The author does not consider radial or angular dependence on shading. Jackson also expands Anderson's definition of canopy shading, treating the canopy not as a single layer, but as 0, 1, or 2 discrete layers, each composed of individual fronds. While this is a significant improvement over Anderson's light model, it is still rather simplistic.

Both Anderson's and Jackson's model were carried out by numerically solving a system of differential equations over small time intervals. In 1990, M.A. Burgman and V.A. Gerard developed a stochastic population model [3]. This approach is quite different, and functions by dividing kelp plants into groups based on size and age and generating random numbers to determine how the population distribution over these groups changes over time based on measured rates of growth, death, decay, light availability, etc. In the same year, Nyman et. al. published a similar model alongside a Markov chain model, and compared the results with experimental data collected in New Zealand [10].

In 1996 and 1998 respectively, P. Duarte and J.G. Ferreira used the size-class approach to create a more general model of macroalgae growth, and Yoshimori et. al. created a differential equation model of *Laminaria religiosa* with specific

emphasis on temperature dependence of growth rate [5, 15]. These were the some of the first models of kelp growth that did not specifically relate to *Macrocystis pyrifera* ("giant kelp"). Initially, there was a great deal of excitement about this species due to it's incredible size and growth rate, but difficulties in harvesting and negative environmental impacts have caused scientists to investigate other kelp species.

1.3   Background on Radiative Transfer

In terms of optical quantities, of primary interest is in the radiance at each point from all directions, which affects the photosynthetic rate of the kelp, and therefore the total amount of biomass producible in a given area as well as the total nutrient remediation potential. The equation governing the radiance throughout the system is known as the Radiative Transfer Equation (RTE), which has been largely unutilized in the fields of oceanography and aquaculture. The Radiative Transfer Equation has been used primarily in stellar astrophysics; it's application to marine biology is fairly recent [9]. In its full form, radiance is a function of 3 spatial dimensions, 2 angular dimensions, and frequency, making for an incredibly complex problem. In this work, frequency is ignored, only monochromatic radiation is considered. The RTE states that along a given path, radiance is decreased by absorption and scattering out of the path, while it is increased by emission and scattering into the path. In our situation, emission is negligible, owing only perhaps to some small luminescent phytoplankton or other anomaly, and can therefore be safely ignored.

Understanding the growth rate and nutrient recovery by kelp cultures has important marine biological implications. For example, recent work by our research group at Clarkson University, the University of Maine, and SINTEF Fisheries and Aquaculture is investigating kelp aquaculture as a means to recover nutrients from wastewater effluent plumes in coastal environments into a valuable biomass feedstock for many products. Current models for kelp growth place little emphasis on the way in which nearby plants shade one another. Self-shading may be a significant model feature, though, as light availability may impact the growth and composition of the kelp biomass, and thus the mixture of goods that may be derived.

1.4 Overview of Thesis

The remainder of this document is organized as follows. In Chapter 2, we develop a probabilistic model to describe the spatial distribution of kelp by assuming simple distributions for the lengths and orientations of fronds. We begin Chapter 3 with a survey of fundamental radiometric quantities and optical properties of matter. We use the spatial kelp distribution from Chapter 2 to determine optical properties of the combined water-kelp medium. We then present the Radiative Transfer Equation, an integro-partial differential equation which describes the the light field as a function of position and angle. An asymptotic expansion is explored for cases where absorption dominates scattering in the medium, such as in very clear water or high kelp density. In Chapter 4, details are given for the numerical solution of the equations from Chapters 2 and 3. Both the full finite difference solution and the asymptotic approx-

imation are described. Next, in Chapter 5, we discuss the availability of necessary parameters in the literature. For those which are not readily available, we give rough estimates and briefly describe experimental methods for their determination. Then, in Chapter 6, we investigate the necessary grid resolution for adequate accuracy in the full finite difference solution and compare to the asymptotic approximation for a few parameter sets. Further, we determine the effect of varying a few key parameters on the light field predicted by the asymptotic approximation. Afterwards, the light model developed here is used in a numerical simulation of kelp growth, and the predicted light field and biomass production are compared to those predicted by a simpler 1D exponential decay light model. Finally, we conclude with Chapter 7 by giving a brief summary of the model, discuss and its performance, and suggest improvements and avenues for future work.

CHAPTER II

KELP MODEL

In order to properly model the spatial distribution of light around the kelp, it is first necessary to formulate a spatial description of the kelp, which we do in this chapter. We take a probabilistic approach to describing the kelp. We begin by describing the distribution of kelp fronds, and through algebraic manipulation, we are able to assign to each point in space a probability that kelp occupies the location.

2.1   Physical Setup

The life of cultivated macroalgae generally begins in the laboratory, where microscopic kelp spores are inoculated onto a thread in a small laboratory pool. This thread is wrapped around a large rope, which is placed in the ocean and generally suspended by buoys in one of two configurations: horizontal or vertical. We consider only the vertical rope case, in which the kelp plants extend radially outward from the rope in all directions. The mature *Saccharina latissima* plant consists of a single frond (leaf), a stipe (stem) and a holdfast (root structure). Plants extending from each rope will shade both themselves and their neighbors to varying degrees based on the depth of the kelp, the rope spacing, the angle of incident light on the surface of the water, and the optical properties of the medium.
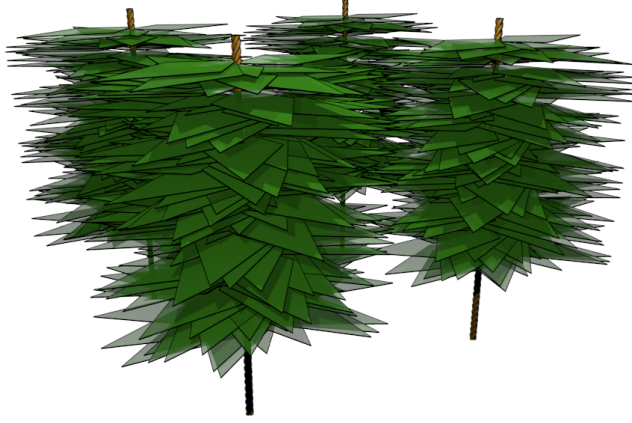
Figure 2.1: Rendering of four nearby vertical kelp ropes

2.2 Coordinate System

Consider the rectangular domain

$$x_{\min} \leq x \leq x_{\max},$$

$$y_{\min} \leq y \leq y_{\max},$$

$$z_{\min} \leq z \leq z_{\max}.$$

For all three dimensional analysis, we use the absolute coordinate system defined in figure 2.2. In the following sections, it is necessary to convert between Cartesian and spherical coordinates, which we do using the relations

$$\begin{cases} x = r \sin\phi \cos\theta, \\ y = r \sin\phi \sin\theta, \\ z = r \cos\phi. \end{cases} \tag{2.1}$$

10

Therefore, for some function $f(x, y, z)$, we can write its derivative along a path in spherical coordinates in terms of Cartesian coordinates using the chain rule.

$$\frac{\partial f}{\partial r} = \frac{\partial f}{\partial x}\frac{\partial x}{\partial r} + \frac{\partial f}{\partial y}\frac{\partial y}{\partial r} + \frac{\partial f}{\partial z}\frac{\partial z}{\partial r}$$

Then, calculating derivatives from (2.1) yields

$$\frac{\partial f}{\partial r} = \frac{\partial f}{\partial x}\sin\phi\cos\theta + \frac{\partial f}{\partial y}\sin\phi\sin\theta + \frac{\partial f}{\partial z}\cos\phi. \tag{2.2}$$
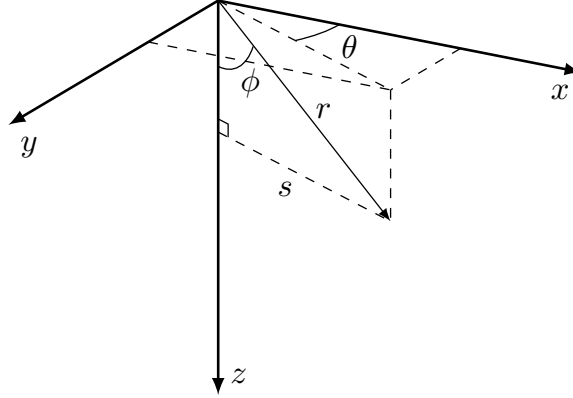
Figure 2.2: Downward-facing right-handed coordinate system with radial distance r from the origin, distance s from the z axis, zenith angle ϕ and azimuthal angle θ

2.3 Population Distributions

2.3.1 Frond Shape

We assume the frond is a kite with length l from base to tip, and width w from left to right. The proximal length is the shortest distance from the base to the diagonal connecting the left and right corners, and is notated as f_a Likewise, the distal length

11
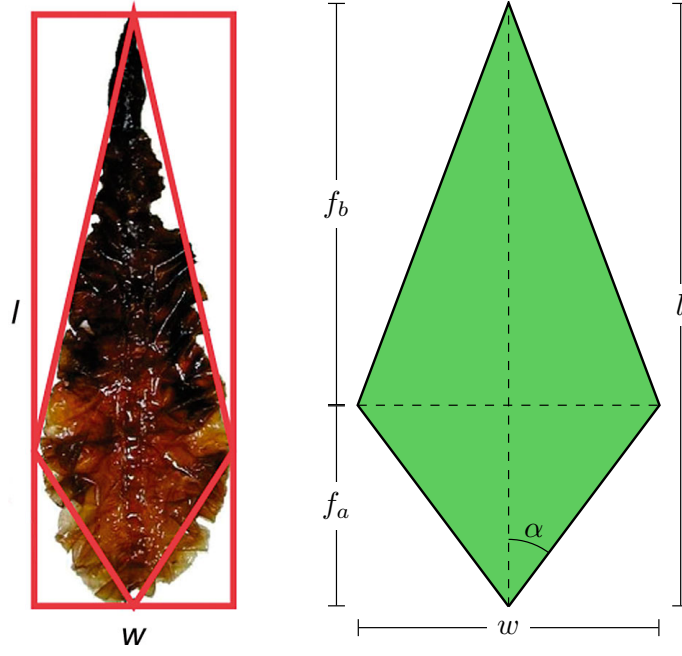
Figure 2.3: Simplified kite-shaped frond

is the shortest distance from that diagonal to the tip, notated f_b. We have

$$f_a + f_b = l$$

When considering a whole population with varying sizes, it is more convenient to specify ratios than absolute lengths. Let the following ratios be defined.

$$f_r = \frac{l}{w}$$

$$f_s = \frac{f_a}{f_b}$$

These ratios are assumed to be consistent among the entire population, making all fronds geometrically similar. With these definitions, the shape of the frond can be fully specified by l, f_r, and f_s. It is possible, then, to redefine w, f_a and f_b as follows from the preceding formulas.

$$w = \frac{l}{f_r}$$

$$f_a = \frac{l f_s}{1 + f_s}$$

$$f_b = \frac{l}{1 + f_s}$$

The angle α, half of the angle at the base corner, is also important in our analysis. Using the above equations,

$$\alpha = \tan^{-1}\left(\frac{2 f_r f_s}{1 + f_s}\right)$$

The area of the frond is given by

$$A = \frac{lw}{2} = \frac{l^2}{2 f_r}.$$

Likewise, if the area is known, then the length is

$$l = \sqrt{2 A f_r} \tag{2.3}$$

2.3.2 Length and Angle Distributions

We assume that frond lengths are normally distributed with mean μ_l and standard deviation σ_l. That is, the frond length distribution has the probability density function (PDF)

$$P_l(l) = \frac{1}{\sqrt{2\pi\sigma_l^2}} \exp\left(\frac{(l - \mu_l)^2}{2\sigma_l^2}\right).$$

We assume the frond angle varies according to the von Mises distribution, which is the periodic analogue of the normal distribution, defined on $[-\pi, \pi]$ rather

13

than $(-\infty, \infty)$. The von Mises distribution has two parameters, μ and κ, which shift and sharpen its peak respectively, as shown in Figure 2.4. κ can be considered analogous to $1/\sigma$ in the normal distribution. Here, we use $\mu = \theta_w$ and $\kappa = v_w$. That is, in the case of zero current velocity, the frond angles are be distributed uniformly, while as current velocity increases, they become increasingly likely to be pointing in the direction of the current. Note that θ_w and v_w vary over depth.

The PDF for the von Mises distribution is

$$P_{\theta_f}(\theta_f) = \frac{\exp\left(v_w \cos(\theta_f - v_w)\right)}{2\pi I_0(v_w)}$$

where $I_0(x)$ is the modified Bessel function of the first kind of order 0. Notice that unlike the normal distribution, the von Mises distribution approaches a *non-zero* uniform distribution as κ approaches 0.

$$\lim_{v_w \to 0} P_{\theta_f}(\theta_f) = \frac{1}{2\pi} \; \forall \, \theta_f \in [-\pi, \pi]$$

2.3.3 Joint Length-Orientation Distribution

The previous two distributions can reasonably be assumed to be independent of one another. That is, the angle of the frond does not depend on the length, or vice versa. Therefore, the probability of a frond simultaneously having a given frond length and angle is the product of their individual probabilities.

Given independent events A and B,

$$P(A \cap B) = P(A)P(B)$$

14
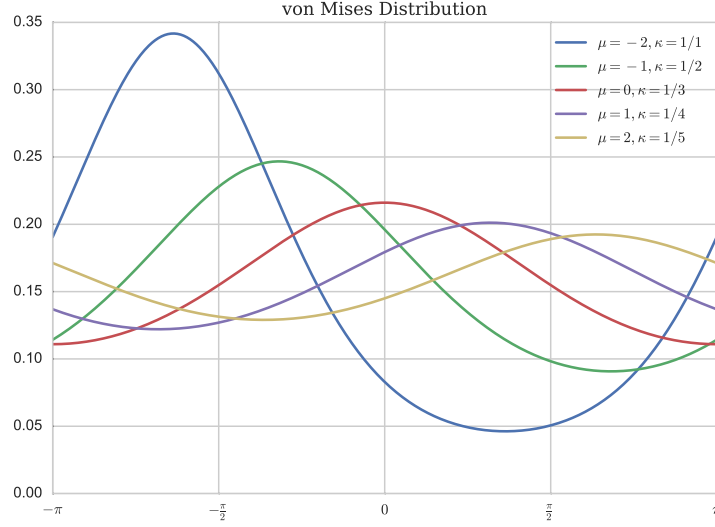
Figure 2.4: von Mises distribution for a variety of parameters

Then the probability of frond length l and frond angle θ_f coinciding is

$$P_{2D}(\theta_f, l) = P_{\theta_f}(\theta_f) \cdot P_l(l)$$

A contour plot of this 2D distribution for a specific set of parameters is shown in figure 2.5, where probability is represented by color in the 2D plane. Darker green represents higher probability, while lighter beige represents lower probability. In figure 2.6, 50 samples are drawn from this distribution and plotted.

It is important to note that if P_{θ_f} were dependent on l, the above definition of P_{2D} would no longer be valid. For example, it might be more realistic to say that larger fronds are less likely to bend towards the direction of the current. In this case, (2.3.3) would no longer hold, and it would be necessary to use the following more

general relation.

$$P(A \cap B) = P(A)P(B|A) = P(B)P(B|A)$$

This is currently not taken into consideration in this model.
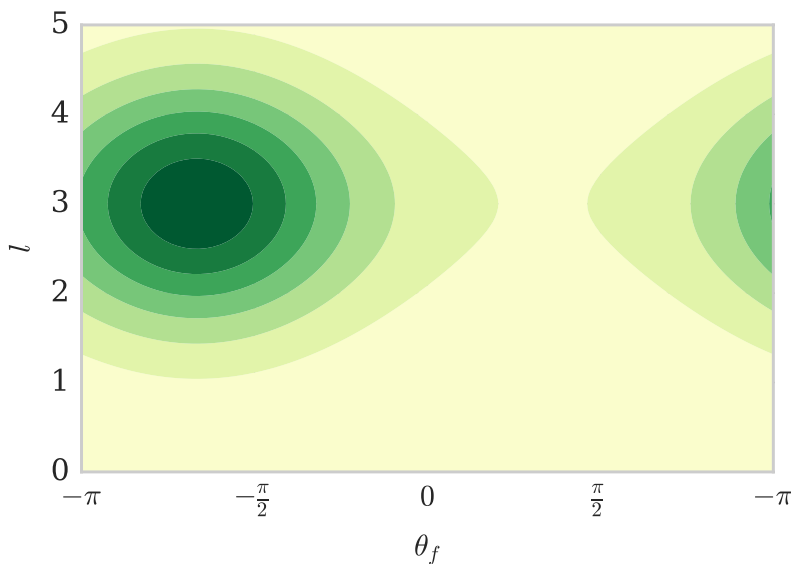
Figure 2.5: 2D length-angle probability distribution with $\theta_w = 2\pi/3, v_w = 1$

2.4   Spatial Distribution

2.4.1   Rotated Coordinate System

To determine under what conditions a frond will occupy a given point, we begin by describing the shape of the frond in Cartesian and then converting to polar coordinates. Of primary interest are the edges connected to the frond tip. For convenience, we will use a rotated coordinate system (θ', s) such that the line connecting the base to the tip is vertical, with the base at $(0, 0)$. The Cartesian analogue of this coordi-
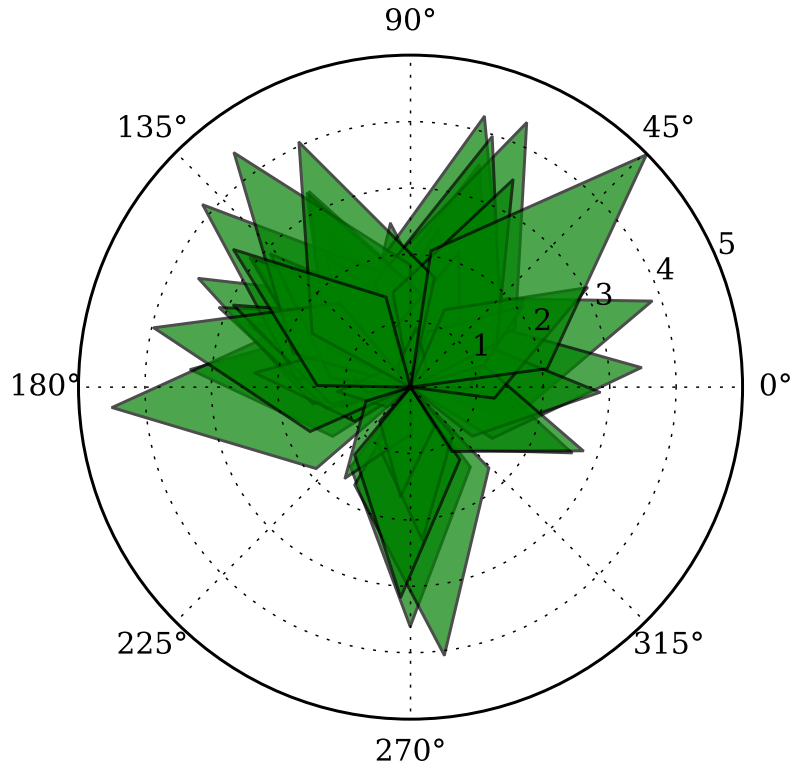
Figure 2.6: A sample of 50 kelp fronds with length and angle picked from the distribution above with $f_s = 0.5$ and $f_r = 2$.

nate system, (x', y'), has the following properties.

$$x' = s\cos\theta'$$

$$y' = s\sin\theta'$$

and

$$s = \sqrt{x'^2 + y'^2}$$

$$\theta' = \text{atan2}(y, x)$$

17

2.4.2 Functional Description of Frond Edge

With this coordinate system established, we can describe the outer two edges of the frond in Cartesian coordinates as a piecewise linear function connecting the left corner: $(-w/2, f_a)$, the tip: $(0, l)$, and the right corner: $(w/2, f_a)$. This function has the form

$$y_f'(x') = l - \text{sign}(x')\frac{f_b}{w/2}x'.$$

Using the equations in Section 2.4.1, this can be written in polar coordinates after some rearrangement as

$$s_f'(\theta') = \frac{l}{\sin\theta' + S(\theta')\frac{2f_b}{w}\cos\theta'}$$

where

$$S(\theta') = \text{sign}(\theta' - \pi/2)$$

Then, using the relationships in Section 2.3.1, we can rewrite the above equation in terms of our frond ratios f_s and f_r.

$$s_f'(\theta') = \frac{l}{\sin\theta' + S(\theta')\frac{2f_r}{1+f_s}\cos\theta'}$$

2.4.3 Absolute Coordinates

To generalize to a frond pointed at an angle θ_f, we will use the coordinate system (θ, s) such that

$$\theta = \theta' + \theta_f - \frac{\pi}{2}$$

18

Then, for a frond pointed at the arbitrary angle θ_f, the function for the outer edges can be written as

$$s_f(\theta) = s'_f\left(\theta - \theta_f + \frac{\pi}{2}\right)$$

2.4.4 Conditions for Occupancy

Consider a fixed frond of length l at an angle θ_f. The point (θ, s) is occupied by the frond if

$$|\theta_f - \theta| < \alpha$$

and

$$s < s_f(\theta)$$

Equivalently, letting the point (θ, s) be fixed, a frond occupies the point if the following conditions are satisfied.

$$\theta - \alpha < \theta_f < \theta + \alpha \tag{2.4}$$

and

$$l > l_{min}(\theta, s) \tag{2.5}$$

where

$$l_{min}(\theta, s) = s \cdot \frac{l}{s_f(\theta)}$$

Then, considering the point to be fixed, (2.4) and (2.5) define the spacial region $R_s(\theta, s)$ called the "occupancy region for (θ, s)" with the property that if the tip of a frond lies within this region (i.e. $(\theta_f, l) \in R_s(\theta, s)$), then it occupies

19

the point. $R_s(3\pi/4, 3/2)$ is shown in blue in figure 2.7 and the smallest possible occupying fronds for several values of θ_f are shown in various colors. Any frond longer than these at the same angle will also occupy the point.
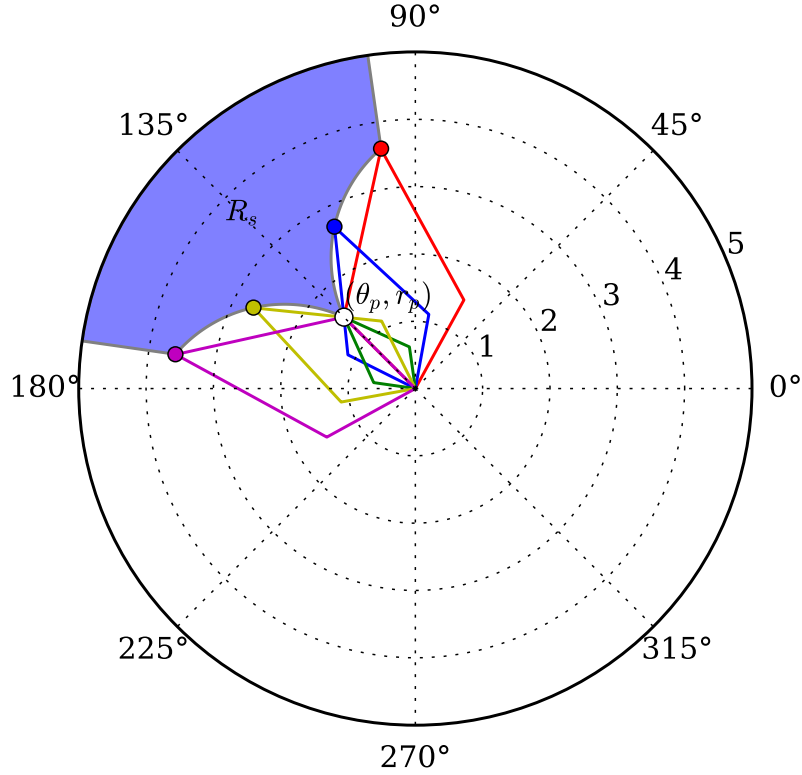
Figure 2.7: Outlines of minimum-length fronds for a variety of angles to occupy the point $(\theta, s) = (3\pi/4, 3/2)$

2.4.5 Probability of Occupancy

We are interested in the probability that, given a fixed point (θ, s), values of l and θ_f chosen from the distributions described in Section 2.3.2 will fall in the occupancy

region. This is found by integrating P_{2D} over the occupancy region for (θ, s), as depicted in figure 2.8.
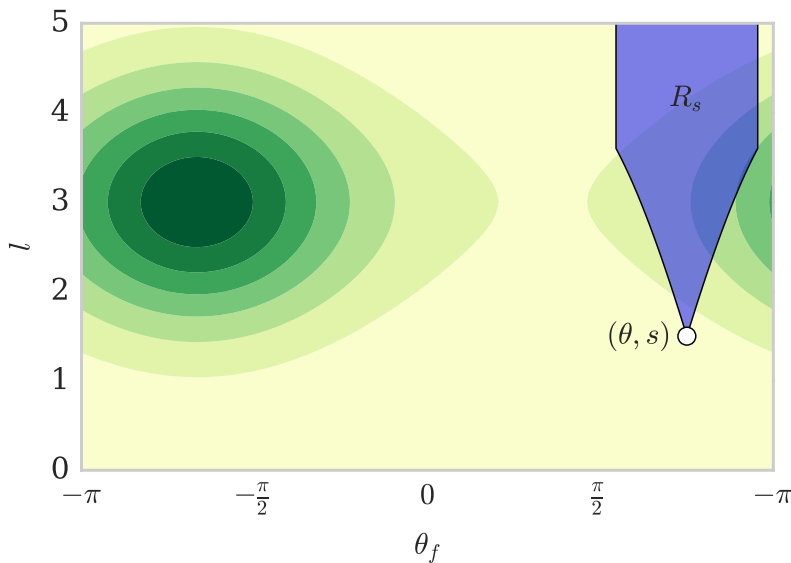
Figure 2.8: Contour plot of $P_{2D}(\theta_f, l)$ overlayed with the region in the $\theta_f - l$ plane which results in a frond occupying the point $(\theta, s) = (3\pi/4, 3/2)$

Now, integrating $P_{2D}(\theta_f, l)$ over $R_s(\theta, s)$ yields the proportion of the population occupying the point (θ, s).

$$
\begin{aligned}
\tilde{P}_k(\theta, s, z) &= \iint_{R_s(\theta,s)} P_{2D}(\theta_f, l) \, dl \, d\theta_f \\
&= \int_{\theta-\alpha}^{\theta+\alpha} \int_{l_{min}(\theta_f)}^{\infty} P_{2D}(\theta_f, l) \, dl \, d\theta_f
\end{aligned}
$$

Then, multiplying $\tilde{P}_k$ by the number of fronds in the population n of the depth layer gives the expected number of fronds occupying the point. Now, assuming a uniform thickness t for all fronds, and a thickness dz of the depth layer, we find

the proportion of the grid cell occupied by kelp to be

$$P_k = \frac{nt}{dz}\tilde{P}_k.$$

Then, the effective absorption coefficient can be calculated at any point in space as

$$a(\boldsymbol{x}) = P_k(\boldsymbol{x})a_k + (1 - P_k(\boldsymbol{x}))a_w$$
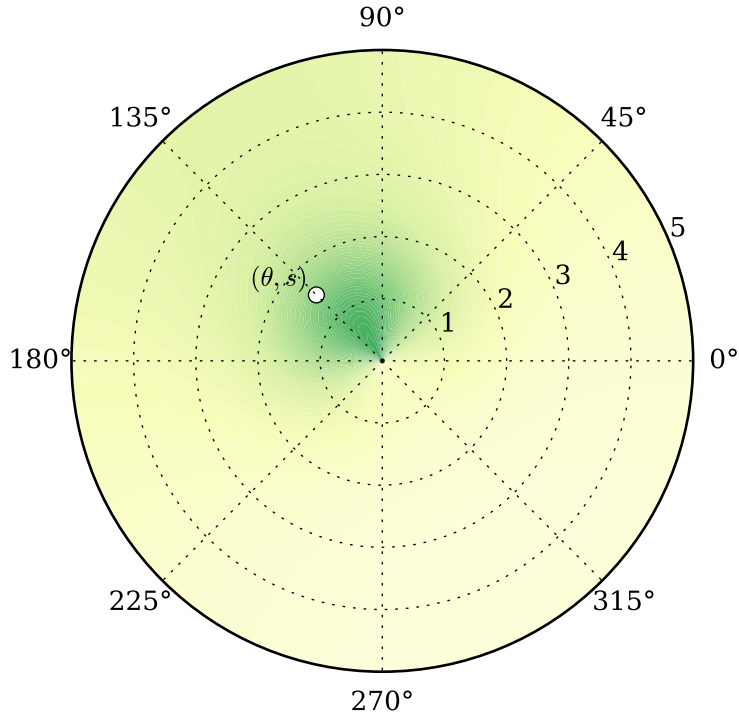
Figure 2.9: Contour plot of the probability of occupying sampled at 121 points using $\theta_f = 2\pi/3, v_w = 1$

CHAPTER III

LIGHT MODEL

Now that we have formulated the distribution of kelp throughout the medium, we introduce the Radiative Transfer Equation, which is used to calculate the light field.

3.1 Optical Definitions

3.1.1 Radiometric Quantities

One of the most fundamental quantities in optics is radiant flux Φ, which is the has units of energy per time. The quantity of primary interest in modeling the light field is radiance L, which is defined as the radiant flux per steradian per projected surface area perpendicular to the direction of propagation of the beam. That is,

$$L = \frac{d^2\Phi}{dA d\omega}$$

Once the radiance L is calculated everywhere, the irradiance is

$$I(\boldsymbol{x}) = \int_{4\pi} L(\boldsymbol{x}, \boldsymbol{\omega}) \, d\omega.$$

Integrating $I(\boldsymbol{x})$, which has units $\mathrm{W/m^2}$, over the surface of a frond, produces the power (with units W) transmitted to the frond. For details, see Section 4.5.5.

Irradiance is sometimes given in units of moles of photons (a mole of photons is also called an Einstein) per second, with the conversion [8] given by

$$1\,\mathrm{W/m^2} = 4.2\,\mathrm{\mu mol\,photons/s}.$$

3.1.2 Inherent Optical Properties

We must now define a few inherent optical properties (IOPs) which depend only on the medium of propagation. These phenomena are governed by three inherent optical properties (IOPs) of the medium. The absorption coefficient $a(\boldsymbol{x})$ (units $\mathrm{m^{-1}}$) defines the proportional loss of radiance per unit length. The scattering coefficient b (units $\mathrm{m^{-1}}$), defines the proportional loss of radiance per unit length, and is assumed to be constant over space.

The volume scattering function (VSF) $\beta(\Delta) : [-1, 1] \to \mathbb{R}^+$ (units $\mathrm{sr^{-1}}$) defines the probability of light scattering at any given angle from its source. Formally, given two directions $\boldsymbol{\omega}$ and $\boldsymbol{\omega}'$, $\beta(\boldsymbol{\omega} \cdot \boldsymbol{\omega}')$ is the probability density of light scattering from $\boldsymbol{\omega}$ into $\boldsymbol{\omega}'$ (or vice-versa). Of course, since a single direction subtends no solid angle, the probability of scattering occurring exactly from $\boldsymbol{\omega}$ to $\boldsymbol{\omega}'$ is 0. Rather, we say that the probability of radiance being scattered from a direction ω into an element of solid angle Ω is $\int_\Omega \beta(\boldsymbol{\omega} \cdot \boldsymbol{\omega}')\, d\boldsymbol{\omega}'$.

The VSF is normalized such that

$$\int_{-1}^{1} \beta(\Delta)\, d\Delta = \frac{1}{2\pi},$$

so that for any ω,

$$\int_{4\pi} \beta(\boldsymbol{\omega} \cdot \boldsymbol{\omega}')\, d\boldsymbol{\omega}' = 1.$$

24

i.e., the probability of light being scattered to some direction on the unit sphere is 1.

3.2 The Radiative Transfer Equation

We now present the Radiative Transfer Equation, whose solution is the radiance in the medium as a function of position and angle.

3.2.1 Ray Notation

Consider a fixed position $\boldsymbol{x}$ and direction $\boldsymbol{\omega}$ such that $\boldsymbol{\omega} \cdot \hat{z} \neq 0$. Let $\boldsymbol{l}(\boldsymbol{x}, \boldsymbol{\omega}, s)$ denote the linear path containing $\boldsymbol{x}$ in the direction $\boldsymbol{\omega}$. Assume that the ray is not horizontal. Then, it originates either at the surface or bottom of the domain, with initial z coordinate given by

$$
z_0 = \begin{cases} 0, & \boldsymbol{\omega} \cdot \hat{z} < 0 \\ \\ z_{\text{max}}, & \boldsymbol{\omega} \cdot \hat{z} > 0. \end{cases}
$$

Hence, the ray path is parameterized as

$$
\boldsymbol{l}(\boldsymbol{x}, \boldsymbol{\omega}, s) = \frac{1}{\tilde{s}}(s\boldsymbol{x} + (\tilde{s} - s)\boldsymbol{x_0}(\boldsymbol{x}, \boldsymbol{\omega})), \tag{3.1}
$$

where

$$
\boldsymbol{x_0}(\boldsymbol{x}, \boldsymbol{\omega}) = \boldsymbol{x} - \tilde{s}\boldsymbol{\omega}
$$

is the origin of the ray, and

$$
\tilde{s} = \frac{\boldsymbol{x} \cdot \hat{z} - z_0}{\boldsymbol{\omega} \cdot \hat{z}}
$$

is the path length from $\boldsymbol{x_0}(\boldsymbol{x}, \boldsymbol{\omega})$ to $\boldsymbol{x}$.

25

3.2.2 Colloquial Description

Denote the radiance at $\boldsymbol{x}$ in the direction $\boldsymbol{\omega}$ by $L(\boldsymbol{x}, \boldsymbol{\omega})$. As light travels along $\boldsymbol{l}(\boldsymbol{x}, \boldsymbol{\omega}, s)$, interaction with the medium produces three phenomena of interest:

1. Radiance is decreased due to absorption.

2. Radiance is decreased due to scattering out of the path to other directions.

3. Radiance is increased due to scattering into the path from other directions.

3.2.3 Equation of Transfer

Combining these phenomena yields the Radiative Transfer Equation along $\boldsymbol{l}(\boldsymbol{x}, \boldsymbol{\omega})$,

$$\frac{dL}{ds}(\boldsymbol{l}(\boldsymbol{x}, \boldsymbol{\omega}, s), \boldsymbol{\omega}) = -(a(\boldsymbol{x}) + b)L(\boldsymbol{x}, \boldsymbol{\omega}) + b \int_{4\pi} \beta(\boldsymbol{\omega} \cdot \boldsymbol{\omega}')L(\boldsymbol{x}) \, d\omega', \qquad (3.2)$$

where $\int_{4\pi}$ denotes integration over the unit sphere. The derivative of L over the path can be rewritten as

$$\frac{dL}{ds}(\boldsymbol{l}(\boldsymbol{x}, \boldsymbol{\omega}, s), \boldsymbol{\omega}) = \frac{d\boldsymbol{l}}{ds}(\boldsymbol{x}, \boldsymbol{\omega}, s) \cdot \nabla L(\boldsymbol{x}, \boldsymbol{\omega}', \boldsymbol{\omega})$$

$$= \boldsymbol{\omega} \cdot \nabla L(\boldsymbol{x}, \boldsymbol{\omega}),$$

which unveils the general form of the Radiative Transfer Equation,

$$\boldsymbol{\omega} \cdot \nabla L(\boldsymbol{x}, \boldsymbol{\omega}) = -(a(\boldsymbol{x}) + b)L(\boldsymbol{x}, \boldsymbol{\omega}) + b \int_{4\pi} \beta(\boldsymbol{\omega} \cdot \boldsymbol{\omega}')L(\boldsymbol{x}, \boldsymbol{\omega}') \, d\omega'$$

or, equivalently,

$$\boldsymbol{\omega} \cdot \nabla L(\boldsymbol{x}, \boldsymbol{\omega}) + a(\boldsymbol{x})L(\boldsymbol{x}, \boldsymbol{\omega}) = b \left(\int_{4\pi} \beta(\boldsymbol{\omega} \cdot \boldsymbol{\omega}')L(\boldsymbol{x}, \boldsymbol{\omega}') \, d\omega' - L(\boldsymbol{x}, \boldsymbol{\omega}) \right). \qquad (3.3)$$

3.2.4 Boundary Conditions

We use periodic boundary conditions in the x and y directions,

$$L\left((x_{\min}, y, z), \boldsymbol{\omega}\right) = L\left((x_{\max}, y, z), \boldsymbol{\omega}\right),$$

$$L\left((x, y_{\min}, z), \boldsymbol{\omega}\right) = L\left((x, y_{\max}, z), \boldsymbol{\omega}\right).$$

In the z direction, we specify a spatially uniform downwelling light just under the surface of the water by a function $f(\boldsymbol{\omega})$. Or if $z_{\min} > 0$, then the radiance at $z = z_{\min}$ should be specified instead (as opposed to the radiance at the first grid cell center). Further, we assume that no upwelling light enters the domain from the bottom, so

$$L(\boldsymbol{x_s}, \boldsymbol{\omega}) = f(\omega) \text{ if } \boldsymbol{\omega} \cdot \hat{z} > 0,$$

$$L(\boldsymbol{x_b}, \boldsymbol{\omega}) = 0 \text{ if } \boldsymbol{\omega} \cdot \hat{z} < 0.$$

3.3 Low-Scattering Approximation

In clear waters where absorption is more important than scattering, an asymptotic expansion can be used whereby the light field is generated through a sequence of discrete scattering events.

3.3.1 Asymptotic Expansion

Taking b to be small, we introduce the asymptotic series

$$L(\boldsymbol{x}, \boldsymbol{\omega}) = L_0(\boldsymbol{x}, \boldsymbol{\omega}) + b L_1(\boldsymbol{x}, \boldsymbol{\omega}) + b^2 L_2(\boldsymbol{x}, \boldsymbol{\omega}) + \cdots.$$

Substituting the above into (3.3) yields

$$\boldsymbol{\omega} \cdot \nabla \left[L_0(\boldsymbol{x}, \boldsymbol{\omega}) + b L_1(\boldsymbol{x}, \boldsymbol{\omega}) + b^2 L_2(\boldsymbol{x}, \boldsymbol{\omega}) + \cdots \right]$$

$$+ a(\boldsymbol{x}) \left[L_0(\boldsymbol{x}, \boldsymbol{\omega}) + b L_1(\boldsymbol{x}, \boldsymbol{\omega}) + b^2 L_2(\boldsymbol{x}, \boldsymbol{\omega}) + \cdots \right]$$

$$= b \Bigg(\int_{4\pi} \beta(\boldsymbol{\omega} \cdot \boldsymbol{\omega}') \left[L_0(\boldsymbol{x}, \boldsymbol{\omega}') + b L_1(\boldsymbol{x}, \boldsymbol{\omega}') + b^2 L_2(\boldsymbol{x}, \boldsymbol{\omega}') + \cdots \right] d\boldsymbol{\omega}'$$

$$- \left[L_0(\boldsymbol{x}, \boldsymbol{\omega}) + b L_1(\boldsymbol{x}, \boldsymbol{\omega}) + b^2 L_2(\boldsymbol{x}, \boldsymbol{\omega}) + \cdots \right] \Bigg).$$

Grouping like powers of b, we have the decoupled set of equations

$$\boldsymbol{\omega} \cdot \nabla L_0(\boldsymbol{x}, \boldsymbol{\omega}) + a(\boldsymbol{x}) L_0(\boldsymbol{x}) = 0, \tag{3.4}$$

$$\boldsymbol{\omega} \cdot \nabla L_1(\boldsymbol{x}, \boldsymbol{\omega}) + a(\boldsymbol{x}) L_1(\boldsymbol{x}) = \int_{4\pi} \beta(\boldsymbol{\omega} \cdot \boldsymbol{\omega}') L_0(\boldsymbol{x}, \boldsymbol{\omega}') \, d\boldsymbol{\omega}' - L_0(\boldsymbol{x}, \boldsymbol{\omega}),$$

$$\boldsymbol{\omega} \cdot \nabla L_2(\boldsymbol{x}, \boldsymbol{\omega}) + a(\boldsymbol{x}) L_2(\boldsymbol{x}) = \int_{4\pi} \beta(\boldsymbol{\omega} \cdot \boldsymbol{\omega}') L_1(\boldsymbol{x}, \boldsymbol{\omega}') \, d\boldsymbol{\omega}' - L_1(\boldsymbol{x}, \boldsymbol{\omega}).$$

$$\vdots$$

In general, for $n \geq 1$,

$$\boldsymbol{\omega} \cdot \nabla L_n(\boldsymbol{x}, \boldsymbol{\omega}) + a(\boldsymbol{x}) L_n(\boldsymbol{x}) = \int_{4\pi} \beta(\boldsymbol{\omega} \cdot \boldsymbol{\omega}') L_{n-1}(\boldsymbol{x}, \boldsymbol{\omega}') \, d\boldsymbol{\omega}' - L_{n-1}(\boldsymbol{x}, \boldsymbol{\omega}). \tag{3.5}$$

For boundary conditions, let $\boldsymbol{x_s}$ be a point on the surface of the domain. Then,

$$L_0(\boldsymbol{x_s}, \boldsymbol{\omega}) + b L_1(\boldsymbol{x_s}, \boldsymbol{\omega}) + b^2 L_2(\boldsymbol{x_s}, \boldsymbol{\omega}) + \cdots = \begin{cases} f(\omega), & \hat{z} \cdot \omega > 0 \\ \\ 0, & \text{otherwise,} \end{cases}$$

28

which can be decomposed as

$$L_0(\boldsymbol{x}, \boldsymbol{\omega}) = \begin{cases} f(\boldsymbol{\omega}), & \hat{z} \cdot \boldsymbol{\omega} > 0, \\ \\ 0, & \text{otherwise,} \end{cases} \tag{3.6}$$

$$L_1(\boldsymbol{x}, \boldsymbol{\omega}) = 0$$

$$L_2(\boldsymbol{x}, \boldsymbol{\omega}) = 0.$$

$$\vdots$$

In general, for $n \geq 1$,

$$L_n(\boldsymbol{x}, \boldsymbol{\omega}) = 0. \tag{3.7}$$

3.3.2 Analytical Solution

For all $\boldsymbol{x}, \boldsymbol{\omega}$, we consider the path $l(\boldsymbol{x}, \boldsymbol{\omega}, s)$ from (3.1). We extract the absorption coefficient along the path,

$$\tilde{a}(s) = a(\boldsymbol{l}(\boldsymbol{x}, \boldsymbol{\omega}), s).$$

Then, the first equation from the asymptotic expansion, (3.4) and its associated boundary condition, (3.6), can be rewritten as

$$\begin{cases} 0 = \dfrac{du_0}{ds}(s) + \tilde{a}(s)u_0(s) \\ \\ u_0(0) = f(\boldsymbol{\omega}), \end{cases}$$

which we can solve by multiplying by the appropriate integrating factor, as follows.

$$0 = \exp\left(\int_0^s \tilde{a}(s')\,ds'\right)\frac{du_0}{ds} + \exp\left(\int_0^s \tilde{a}(s')\,ds'\right)\tilde{a}(s)u_0(s)$$

$$= \frac{d}{ds}\left[\exp\left(\int_0^s \tilde{a}(s')\,ds'\right)u_0(s)\right].$$

29

Then, integrating both sides yields

$$0 = \int_0^s \frac{d}{ds'} \left[\exp\left(\int_0^{s'} \tilde{a}(s'') \, ds'' \right) u_0(s') \right] ds'$$

$$= \exp\left(\int_0^s \tilde{a}(s') \, ds' \right) u_0(s) - f(\boldsymbol{\omega}).$$

Hence,

$$u_0(s) = f(\omega) \exp\left(-\int_0^s \tilde{a}(s) \, ds \right). \tag{3.8}$$

Then, we convert back from path length s to the spatial coordinate $\boldsymbol{x}$ using

$$L_0(\boldsymbol{l}(\boldsymbol{x}, \boldsymbol{\omega}, s), \boldsymbol{\omega}) = u_0(s).$$

The $n \geq 1$ equations have a nonzero right-hand side, which we call the effective source, $g_n(s)$. This can be similarly extracted along a ray path as

$$g_n(s) = \int_{4\pi} \beta(\boldsymbol{\omega} \cdot \boldsymbol{\omega}') L_{n-1}(\boldsymbol{l}(\boldsymbol{x}, \boldsymbol{\omega}', s), \boldsymbol{\omega}') \, d\boldsymbol{\omega}' - L_{n-1}(\boldsymbol{l}(\boldsymbol{x}, \boldsymbol{\omega}, s), \boldsymbol{\omega}).$$

Then, since g_n depends only on L_{n-1}, it is independent of u_n, which allows (3.5) and its boundary condition, (3.7), to be written as the first order, linear ordinary differential equation along the ray path,

$$\begin{cases} g_n(s) = \dfrac{du_n}{ds}(s) + \tilde{a}(s)u_n(s) \\[2mm] u_n(0) = 0 \end{cases}$$

As with the $n = 0$ equation, the solution is found by multiplying by the appropriate integrating factor.

$$\exp\left(\int_0^s \tilde{a}(s') \, ds' \right) g_n(s) = \exp\left(\int_0^s \tilde{a}(s') \, ds' \right) \frac{du_n}{ds} + \exp\left(\int_0^s \tilde{a}(s') \, ds' \right) \tilde{a}(s)u_n(s)$$

$$= \frac{d}{ds} \left[\exp\left(\int_0^s \tilde{a}(s') \, ds' \right) u_n(s) \right].$$

Integrating both sides yields

$$\int_0^s \exp\left(\int_0^{s'} \tilde{a}(s'')\,ds''\right) g_n(s')\,ds' = \int_0^s \frac{d}{ds'}\left[\exp\left(\int_0^{s'} \tilde{a}(s'')\,ds''\right) u_n(s')\right] ds'$$

$$= \exp\left(\int_0^s \tilde{a}(s')\,ds'\right) u_n(s).$$

Hence,

$$u_n(s) = \exp\left(-\int_0^s \tilde{a}(s')\,ds'\right)\int_0^s \exp\left(\int_0^{s'} \tilde{a}(s'')\,ds''\right) g_n(s')\,ds',$$

which simplifies to

$$u_n(s) = \int_0^s g_n(s')\exp\left(-\int_{s''}^{s'} \tilde{a}(s'')\,ds''\right) ds'. \tag{3.9}$$

As before, the conversion back to spatial coordinates is

$$L_n(\boldsymbol{l}(\boldsymbol{x}, \boldsymbol{\omega}, s), \boldsymbol{\omega}) = u_n(s).$$

CHAPTER IV

NUMERICAL SOLUTION

In this chapter, the mathematical details involved in the numerical solution of the previously described equations are presented. It is assumed that this model is run in conjunction with a model describing the growth of kelp over its life cycle, which calls this light model periodically to update the light field.

4.1   Super-Individuals

The algorithm described in this chapter has two components. First, a probabilistic description of the kelp is generated at each point in a discrete spatial grid. Second, optical properties of the resulting kelp-water medium are derived, and the light field is calculated. The first component is described here.

4.1.1   Frond Length Distribution

Rather than model each kelp frond, a subset of the population, called super-individuals, are modeled explicitly, and are considered to represent many identical individuals, as in [12]. Specifically, at each depth k, there are n super-individuals, indexed by i. Super-individual i has a frond area A_{ki} and represents n_{ki} individual fronds.

From (2.3), the frond length of the super-individual is $l_{ki} = \sqrt{2A_{ki}f_r}$. Given the super-individual data, we calculate the mean μ and standard deviation σ frond lengths using the formulas:

$$\mu_k = \frac{\displaystyle\sum_{i=1}^{N} l_{ki}}{\displaystyle\sum_{i=1}^{N} n_{ki}},$$

$$\sigma_k = \frac{\displaystyle\sum_{i=1}^{N} (l_{ki} - \mu_k)^2}{\displaystyle\sum_{i=1}^{N} n_{ki}}.$$

We then assume that frond lengths are normally distributed in each depth layer with mean μ_k and standard deviation σ_k.

4.2 Discrete Grid

The following is a description of the spatial-angular grid used in the numerical implementation of this model. It is assumed that all simulated quantities are constant over the interior of a grid cell. Other legitimate choices of grids exists; this one was chosen for its relative simplicity.

The domain of the radiative transfer equation is embedded in five dimensions: three spatial (x, y, and z) and two angular (azimuthal θ and polar ϕ). The number of grid cells in each dimension are denoted by n_x, n_y, n_z, n_θ, and n_ϕ, with uniform spacings dx, dy, dz, $d\theta$, and $d\phi$ between adjacent grid points.

The following indices are assigned to each dimension:

$$x \to i$$

$$y \to j$$

$$z \to k$$

$$\theta \to l$$

$$\phi \to m$$

It is convenient, however, to use a single index p to refer to directions $\boldsymbol{\omega}$ rather than referring to θ and ϕ separately. Then, the center of a generic grid cell will be denoted as $(x_i, y_j, z_k, \boldsymbol{\omega}_p)$, and the boundaries between adjacent grid cells will be referred to as *edges*. One-indexing is employed throughout this document.
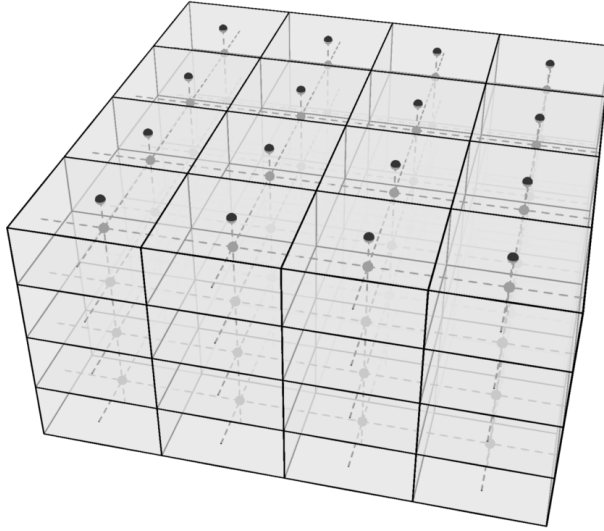
Figure 4.1: Spatial grid

Each spatial grid cell is the Cartesian product of x, y, and z intervals of width dx, dy, and dz respectively. The three-dimensional interval centered at (x_i, y_j, z_k) is denoted X_{ijk}, and has volume $|X_{ijk}| = dx\,dy\,dz$. Also, note that no grid center is located on the plane $z = 0$; the surface radiance boundary condition is treated separately.
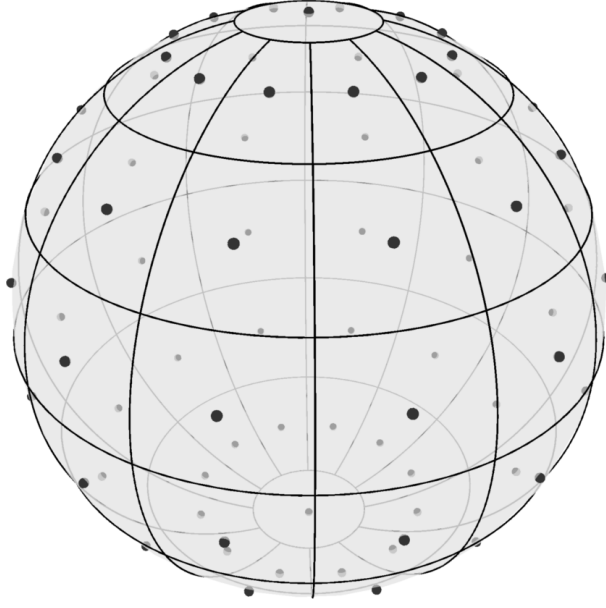
Figure 4.2: Angular grid at each point in space

As shown in Figure 4.2, $\phi = 0$ and $\phi = \pi$, called the north $(+z)$ and south $(-z)$ poles respectively, are treated separately from other angular grid cells. A generic interior angular grid cell centered at $\boldsymbol{\omega}_p$ is the Cartesian product of an azimuthal interval of width $d\theta$ and a polar interval of width $d\theta$. However, two pole cells are the Cartesian product of a polar interval of width $d\phi/2$ and the full azimuthal domain, $[0, 2\pi)$.

With this configuration, the total number of angles considered is $n_{\boldsymbol{\omega}} = n_\theta(n_\phi - 2) + 2$. Then, cells are indexed by $p = 1, \ldots, n_{\boldsymbol{\omega}}$ and are ordered such that $p = 1$ and $p = n_{\boldsymbol{\omega}}$ refer to the north and south poles respectively, $p \le n_{\boldsymbol{\omega}}/2$ refers to the northern hemisphere, and $p > n_{\boldsymbol{\omega}}/2$ refers to the southern hemisphere. Further, the symbol Ω_p is used to refer to the two dimension angular interval centered at ω_p. The solid angle subtended by Ω_p is denoted $|\Omega_p|$. Refer to Appendix A for a more rigorous discussion of the discrete spatial-angular grid.

4.3   Quadrature Rules

Since it is assumed that all quantities are constant within a spatial-angular grid cell, the midpoint rule is employed for both spatial and angular integration. Presented here is a basic derivation of the formulas for integration in the spatial-angular grid. Further details are found in Appendix B.

Define the *spatial characteristic function*

$$\mathcal{X}_{ijk}^X(\boldsymbol{x}) = \begin{cases} 1, & \boldsymbol{x} \in X_{ijk} \\ 0, & \text{otherwise} \end{cases}$$

and the *angular characteristic function*

$$\mathcal{X}_p^\Omega(\boldsymbol{\omega}) = \begin{cases} 1, & \boldsymbol{\omega} \in \Omega_p \\ 0, & \text{otherwise.} \end{cases}$$

36

4.3.1 Spatial Quadrature

The double integral of a function $f(\boldsymbol{x})$ over a depth layer k is approximated as

$$\int_{x_{\min}}^{x_{\max}} \int_{y_{\min}}^{y_{\max}} f(x, y, z_k)\, dy\, dx \approx \int_{x_{\min}}^{x_{\max}} \int_{y_{\min}}^{y_{\max}} \sum_{i=1}^{n_x} \sum_{j=1}^{n_y} \mathcal{X}_{ijk}^{X}(x, y, z_k) f(x_i, y_j, z_k)\, dy\, dx$$

$$= \sum_{i=1}^{n_x} \sum_{j=1}^{n_y} f(x_i, y_j, z_k) \int_{x_{\min}}^{x_{\max}} \int_{y_{\min}}^{y_{\max}} \mathcal{X}_{ijk}^{X}(x, y, z_k)\, dy\, dx$$

$$= \sum_{i=1}^{n_x} \sum_{j=1}^{n_y} |X_{ijk}|\, f(x_i, y_j, z_k)$$

$$= dx\, dy\, dx \sum_{i=1}^{n_x} \sum_{j=1}^{n_y} f(x_i, y_j, z_k).$$

The path integral of $f(\boldsymbol{x})$ over a path $\boldsymbol{l}(s)$ from $s = 0$ to $s = \tilde{s}$ is

$$\int_{0}^{\tilde{s}} f(\boldsymbol{l}(s))\, ds = \sum_{ijk} f(x_i, y_j, z_k)\, ds_{ijk},$$

where ds_{ijk} is the total path distance of $\boldsymbol{l}(s)$ through X_{ijk}. Full details of the path integral algorithm for the case of straight line paths are found in Appendix B.

4.3.2 Angular Quadrature

Then, the integral of a function $f(\boldsymbol{\omega})$ is approximated as

$$\int_{4\pi} f(\boldsymbol{\omega})\, d\boldsymbol{\omega} \approx \int_{4\pi} \sum_{p=1}^{n_\omega} f(\boldsymbol{\omega}_p) \mathcal{X}_p^{\Omega}(\boldsymbol{\omega})\, d\boldsymbol{\omega}$$

$$= \sum_{p=1}^{n_\omega} f(\boldsymbol{\omega}_p) \int_{4\pi} \mathcal{X}_p^{\Omega}(\boldsymbol{\omega})\, d\boldsymbol{\omega}$$

$$= \sum_{p=1}^{n_\omega} f(\boldsymbol{\omega}_p) \int_{\Omega_p} d\boldsymbol{\omega}$$

$$= \sum_{p=1}^{n_\omega} f(\boldsymbol{\omega}_p) \, |\Omega_p| \, .$$

37

4.4 Numerical Asymptotics

Presented here are details of the evaluation of the asymptotic approximations (3.8) and (3.9) to the raditiave transfer equation (3.3).

4.4.1 Scattering Integral

Specifically, the amount of light scattered between angular grid cells is found by integrating β as follows. Consider two angular grid cells, Ω and Ω'. The average probability density of scattering from $\boldsymbol{\omega} \in \Omega$ to $\boldsymbol{\omega}' \in \Omega'$ (or vice versa) is

$$\beta_{pp'} = \frac{1}{|\Omega|\,|\Omega'|} \int_{\Omega} \int_{\Omega'} \beta(\boldsymbol{\omega} \cdot \boldsymbol{\omega}')\, d\boldsymbol{\omega}'\, d\boldsymbol{\omega}$$

Denote the radiance at $(x_i, y_j, z_k, \boldsymbol{\omega}_p)$ by L_{ijkp}. Then, the total radiance scattered into Ω_p from $\Omega_{p'}$ is

$$\int_{\Omega} \int_{\Omega'} \beta(\boldsymbol{\omega} \cdot \boldsymbol{\omega}') L(\boldsymbol{x}, \boldsymbol{\omega}')\, d\boldsymbol{\omega}'\, d\boldsymbol{\omega} = L_{ijkp'} \int_{\Omega} \int_{\Omega_{p'}} \beta(\boldsymbol{\omega} \cdot \boldsymbol{\omega}')\, d\boldsymbol{\omega}'\, d\boldsymbol{\omega}$$

$$= \beta_{pp'}\, |\Omega|\, |\Omega'|\, L_{ijkp'}.$$

Hence, the average radiance scattered is $\beta_{pp'}\, |\Omega'|\, L_{ijkp'}$.

4.4.2 Ray Integral

Given a position $\boldsymbol{x}$ and direction $\boldsymbol{\omega}$, a path through the discrete grid can be constructed as described in Appendix B, from which we can extract piecewise constant variations of the path absorption coefficient, $\tilde{a}(s)$ and the effective source, $g_n(s)$ from Section 3.3.2. Then, we proceed as follows.

* Here are the equations for calculating the double integral over ray paths required for the asymptotics. It will hopefully make more sense once I add words to accompany the symbols.

Let

$$g_n(s) = \sum_{i=1}^{N-1} g_{ni} \mathcal{X}_i(s)$$

$$\tilde{a}(s) = \sum_{i=1}^{N-1} \tilde{a}_i \mathcal{X}_i(s)$$

and

$$\mathcal{X}_i(s) = \begin{cases} 1, & a_I \leq s < s_{i+1} \\ \\ 0, & \text{otherwise} \end{cases}$$

and $\{s_i\}_{i=1}^{N}$ is increasing.

Let $ds_i = s_{i+1} - s_i$.

Let $\hat{i}(s) = \min\{i \in \{1, \dots, N\} : s_i > s\}$. Let $\tilde{d}(s) = s_{\hat{i}(s)} - s$.

We have $s_1 = 0$ and $s_N = \tilde{s}$.

$$u_n(\tilde{s}) = \int_0^{\tilde{s}} g_n(s') \exp\left(-\int_{s''}^{s'} \tilde{a}(s'') \, ds''\right) ds'$$

$$= \int_0^{s_N} \sum_{i=1}^{N-1} g_{ni} \mathcal{X}_i(s') \exp\left(-\int_{s''}^{s'} \sum_{j=1}^{N-1} \tilde{a}_j \mathcal{X}_j(s'') \, ds''\right) ds'$$

$$= \sum_{i=1}^{N-1} g_{ni} \int_0^{s_N} \mathcal{X}_i(s') \exp\left(-\sum_{j=1}^{N-1} \tilde{a}_j \int_{s''}^{s'} \mathcal{X}_j(s'') \, ds''\right) ds'$$

$$= \sum_{i=1}^{N-1} g_{ni} \int_{s_i}^{s_{i+1}} \exp\left(-\tilde{a}_{\hat{i}(s')-1} \tilde{d}(s') - \sum_{j=\hat{i}(s')}^{N-1} \tilde{a}_j ds_j\right) ds'$$

$$= \sum_{i=1}^{N-1} g_{ni} \int_{s_i}^{s_{i+1}} \exp\left(-\tilde{a}_i (s_{i+1} - s') - \sum_{j=i+1}^{N-1} \tilde{a}_j ds_j\right) ds'$$

Let

$$b_i = -\tilde{a}_i s_{i+1} - \sum_{j=i+1}^{N-1} \tilde{a}_j ds_j.$$

Then,

$$u_n(\tilde{s}) = \sum_{i=1}^{N-1} g_{ni} \int_{s_i}^{s_{i+1}} \exp\left(\tilde{a}_i s' + b_i\right) ds'$$

$$= \sum_{i=1}^{N-1} g_{ni} e^{b_i} \int_{s_i}^{s_{i+1}} \exp\left(\tilde{a}_i s'\right) ds'$$

Let

$$d_i = \int_{s_i}^{s_{i+1}} \exp\left(\tilde{a}_i s'\right) ds'$$

$$= \begin{cases} ds_i, & \tilde{a} = 0 \\[2ex] \left(\exp(\tilde{a}_i s_{i+1}) - \exp(\tilde{a}_i s_i)\right) / \tilde{a}_i, & \text{otherwise} \end{cases}$$

Then,

$$u_n(\tilde{s}) = \sum_{i=1}^{N-1} g_{ni} d_i e^{b_i}$$

40

4.5 Finite Difference

We now discuss the discretization of derivatives on the spatial grid.

4.5.1 Discretization

For the spatial interior of the domain, we use the second order central difference formula (CD2) to approximate the derivatives, which is

$$f'(x) = \frac{f(x+dx) - f(x-dx)}{2dx} + \mathcal{O}(dx^3). \tag{CD2}$$

When applying the PDE on the upper or lower boundary, we use the forward and backward difference (FD2 and BD2) formulas respectively. Omitting $\mathcal{O}(dx^3)$, we have

$$f'(x) = \frac{-3f(x) + 4f(x+dx) - f(x+2dx)}{2dx} \tag{FD2}$$

$$f'(x) = \frac{3f(x) - 4f(x-dx) + f(x-2dx)}{2dx} \tag{BD2}$$

For the upper and lower boundaries, we need an asymmetric finite difference method. In general, the Taylor Series of a function f about x is

$$f'(x+\varepsilon) = \sum_{n=1}^{\infty} \frac{f^{(n)}(x)}{n!} \varepsilon^n$$

Truncating after the first few terms, we have

$$f'(x+\varepsilon) = f(x) + f'(x)\varepsilon + \frac{f''(x)}{2}\varepsilon^2 + \mathcal{O}(\varepsilon^3) \tag{4.1}$$

Similarly, replacing ε with $-\varepsilon/2$ we have

$$f'(x - \frac{\varepsilon}{2}) = f(x) - \frac{f'(x)\varepsilon}{2} + \frac{f''(x)\varepsilon^2}{8} + \mathcal{O}(\varepsilon^3). \tag{4.2}$$

41

Rearranging (4.1) produces

$$f''(x)\varepsilon^2 = 2f(x+\varepsilon) - 2f(x) - 2f'(x)\varepsilon + \mathcal{O}(\varepsilon^3) \tag{4.3}$$

Combining (4.2) with (4.3) gives

$$\varepsilon f'(x) = 2f(x) - 2f(x - \frac{\varepsilon}{2}) + f''(x)\frac{\varepsilon^2}{8} + \mathcal{O}(\varepsilon^3)$$

$$= 2f(x) - 2f(x - \frac{\varepsilon}{2}) + \frac{f(x+\varepsilon)}{4} - \frac{f(x)}{4} - \frac{f'(x)\varepsilon}{4} + \mathcal{O}(\varepsilon^3)$$

$$= \frac{4}{5}\left(2f(x) - 2f(x - \frac{\varepsilon}{2}) + \frac{f(x+\varepsilon)}{4} - \frac{f(x)}{4}\right) + \mathcal{O}(\varepsilon^3)$$

Then, dividing by ε gives

$$f'(x) = \frac{-8f(x - \frac{\varepsilon}{2}) + 7f(x) + f(x+\varepsilon)}{5\varepsilon} + \mathcal{O}(\varepsilon^2)$$

Similarly, substituting $\varepsilon \to -\varepsilon$, we have

$$f'(x) = \frac{-f(x - \varepsilon) - 7f(x) + 8f(x + \frac{\varepsilon}{2})}{5\varepsilon} + \mathcal{O}(\varepsilon^2)$$

4.5.2 Difference Equation

In general, we have

$$\boldsymbol{\omega} \cdot \nabla L_p = -(a+b)L_p + \sum_{p'=1}^{n_{\boldsymbol{\omega}}} \beta_{pp'} L_{p'}.$$

Then,

$$\boldsymbol{\omega} \cdot \nabla L_p + (a + b(1 - \beta_{pp'}))L_p - \sum_{p'=1}^{n_{\boldsymbol{\omega}}} \beta_{pp'} L_{p'} = 0$$

Interior:

$$0 = \frac{L_{i+1,jkp} - L_{i-1,jkp}}{2dx} \sin\hat{\phi}_p \cos\hat{\theta}_p$$

$$+ \frac{L_{i,j+1,kp} - L_{i,j-1,kp}}{2dy} \sin\hat{\phi}_p \sin\hat{\theta}_p$$

$$+ \frac{L_{ij,k+1,p} - L_{ij,k-1,p}}{2dz} \cos\hat{\phi}_p$$

$$+ (a_{ijk} + b(1 - \beta_{pp'}))L_{ijkp} - \sum_{p'=1}^{n_\omega} \beta_{pp'} L_{ijkp'}$$

Surface downwelling (BC):

$$0 = \frac{L_{i+1,jkp} - L_{i-1,jkp}}{2dx} \sin\hat{\phi}_p \cos\hat{\theta}_p$$

$$+ \frac{L_{i,j+1,kp} - L_{i,j-1,kp}}{2dy} \sin\hat{\phi}_p \sin\hat{\theta}_p$$

$$+ \frac{-8f_p + 7L_{ijkp} + L_{ij,k+1,p}}{5dz} \cos\hat{\phi}_p$$

$$+ (a_{ijk} + b(1 - \beta_{pp'}))L_{ijkp}$$

$$- \sum_{p'=1}^{n_\omega} \beta_{pp'} L_{ijkp'}.$$

Combining L_{ijkp} terms on the left and moving the boundary condition to the

right gives

$$\frac{L_{i+1,jkp} - L_{i-1,jkp}}{2dx} \sin\hat{\phi}_p \cos\hat{\theta}_p$$

$$+ \frac{L_{i,j+1,kp} - L_{i,j-1,kp}}{2dy} \sin\hat{\phi}_p \sin\hat{\theta}_p$$

$$+ \frac{L_{ij,k+1,p}}{5dz} \cos\hat{\phi}_p$$

$$+ (a_{ijk} + b(1 - \beta_{pp'}) + \frac{7}{5dz} \cos\hat{\phi}_p)L_{ijkp}$$

$$- \sum_{p'=1}^{n_\omega} \beta_{pp'} L_{ijkp'} = \frac{8f_p}{5dz} \cos\hat{\phi}_p.$$

Likewise for the bottom boundary condition, we have

$$0 = \frac{L_{i+1,jkp} - L_{i-1,jkp}}{2dx} \sin \hat{\phi}_p \cos \hat{\theta}_p$$

$$+ \frac{L_{i,j+1,kp} - L_{i,j-1,kp}}{2dy} \sin \hat{\phi}_p \sin \hat{\theta}_p$$

$$- \frac{L_{ij,k-1,p}}{5dz} \cos \hat{\phi}_p$$

$$+ (a_{ijk} + b(1 - \beta_{pp'}) - \frac{7}{5dz} \cos \hat{\phi}_p) L_{ijkp}$$

$$- \sum_{p'=1}^{n_{\omega}} \beta_{pp'} L_{ijkp'}.$$

Now, for upwelling light at the first depth layer (non-BC), we apply FD2.

$$0 = \frac{L_{i+1,jkp} - L_{i-1,jkp}}{2dx} \sin \hat{\phi}_p \cos \hat{\theta}_p$$

$$+ \frac{L_{i,j+1,kp} - L_{i,j-1,kp}}{2dy} \sin \hat{\phi}_p \sin \hat{\theta}_p$$

$$+ \frac{-3L_{ijkp} + 4L_{ij,k+1,p} - L_{ij,k+2,p}}{2dz} \cos \hat{\phi}_p$$

$$+ (a_{ijk} + b(1 - \beta_{pp'})) L_{ijkp}$$

$$- \sum_{p'=1}^{n_{\omega}} \beta_{pp'} L_{ijkp'}.$$

Grouping L_{ijkp} terms gives

$$0 = \frac{L_{i+1,jkp} - L_{i-1,jkp}}{2dx} \sin \hat{\phi}_p \cos \hat{\theta}_p$$

$$+ \frac{L_{i,j+1,kp} - L_{i,j-1,kp}}{2dy} \sin \hat{\phi}_p \sin \hat{\theta}_p$$

$$+ \frac{4L_{ij,k+1,p} - L_{ij,k+2,p}}{2dz} \cos \hat{\phi}_p$$

$$+ \left(a_{ijk} + b(1 - \beta_{pp'}) - 3\frac{\cos \hat{\phi}_p}{2dz} \right) L_{ijkp}$$

$$- \sum_{p'=1}^{n_{\omega}} \beta_{pp'} L_{ijkp'}.$$

Similarly, for downwelling light at the lowest depth layer, we have

$$
\begin{aligned}
0 = {} & \frac{L_{i+1,jkp} - L_{i-1,jkp}}{2dx} \sin \hat{\phi}_p \cos \hat{\theta}_p \\
& + \frac{L_{i,j+1,kp} - L_{i,j-1,kp}}{2dy} \sin \hat{\phi}_p \sin \hat{\theta}_p \\
& + \frac{-4L_{ij,k-1,p} + L_{ij,k-2,p}}{2dz} \cos \hat{\phi}_p \\
& + \left(a_{ijk} + b(1 - \beta_{pp'}) + 3\frac{\cos \hat{\phi}_p}{2dz} \right) L_{ijkp} \\
& - \sum_{p'=1}^{n_{\boldsymbol{\omega}}} \beta_{pp'} L_{ijkp'}
\end{aligned}
$$

4.5.3   Structure of Linear System

Describe layout of matrix.

Derivative case	# nonzero/row	# of rows
interior	$n_{\boldsymbol{\omega}} + 6$	$n_x n_y (n_z - 2) n_{\boldsymbol{\omega}}$
surface downwelling	$n_{\boldsymbol{\omega}} + 5$	$n_x n_y n_{\boldsymbol{\omega}}/2$
bottom upwelling	$n_{\boldsymbol{\omega}} + 5$	$n_x n_y n_{\boldsymbol{\omega}}/2$
surface upwelling	$n_{\boldsymbol{\omega}} + 6$	$n_x n_y n_{\boldsymbol{\omega}}/2$
bottom downwelling	$n_{\boldsymbol{\omega}} + 6$	$n_x n_y n_{\boldsymbol{\omega}}/2$

Table 4.1: Breakdown of nonzero matrix elements by derivative case

Number of rows/columns: $n_x n_y n_z n_{\boldsymbol{\omega}}$

Number of nonzero RHS entries: $n_x n_y n_z/2$

Total number of nonzero matrix entries: $n_x n_y n_{\boldsymbol{\omega}} \left[n_z (n_{\boldsymbol{\omega}} + 6) - 1 \right]$

4.5.4 GMRES

GMRES is a Krylov Subspace method. These work like this. Here's what's special about GMRES. Advantages. Drawbacks. Not practical for running in SINMOD.

4.5.5 Perceived Irradiance

The average irradiance experienced by a kelp frond in depth layer k is

$$\tilde{I}_k = \frac{\sum_{ij} P_{ijk} I_{ijk}}{\sum_{ij} P_{ijk}}.$$

The irradiance perceived by the kelp is expected to be slightly lower than the average irradiance,

$$\bar{I}_k = \frac{\sum_{ij} I_{ijk}}{n_x n_y}$$

since the kelp is more densely located at the center of the domain where the light field is reduced, whereas the simple average is influenced by regions of higher irradiance at the edges of the domain where kelp is not present.

CHAPTER V

PARAMETER VALUES

I'll describe what one would do in order to determine "frond bending coefficients", as well as optical properties of water and kelp, citing literature and reporting values obtained by others.

5.1 Parameters from Literature

* More to come

5.2 Frond Distribution Parameters

5.2.1 Rotation

5.2.2 Lift

Parameter Name	Symbol	Value(s)	Citation	Notes
Kelp Absorptance	A_k	0.8	[4]	Actually for *Macrocystis Pyrifera*
Water absorption coefficient	a_w	?	?	?
Scattering coefficient	b	0.366	[13]	Table 2, $b_{\lambda 0}$, mean
VSF	β	tabulated	[11, 13],	Currently using Petzold
Frond thickness	t	0.4 mm	Ole Jacob	Carina? ***
Water absorption coefficient	a_w	0.03 1 1/m	[6]	Fig. 6, dense cluster. Sannanger Fjord, Western Norway.
Water scattering coefficient	a_w	0.5 1 1/m	[6]	Fig. 7, dense cluster. Sannanger Fjord, Western Norway.
Surface solar irradiance	I_0	$50\,\mathrm{W\,m^{-2}}$	[2]	Irradiance for maximal photosynthesis, converted from photons

Site	$a(\text{m}^{-1})$	$b(\text{m}^{-1})$	$c(\text{m}^{-1})$	a/c	b/c
AUTEC 7	0.082	0.117	0.199	0.412	0.588
AUTEC 8	0.114	0.037	0.151	0.753	0.247
AUTEC 9	0.122	0.043	0.165	0.742	0.258
HAOCE 5	0.195	0.275	0.47	0.415	0.585
HAOCE 11	0.179	0.219	0.398	0.449	0.551
NUC 2200	0.337	1.583	1.92	0.176	0.824
NUC 2040	0.366	1.824	2.19	0.167	0.833
NUC 2240	0.125	1.205	1.33	0.094	0.906
Filtered Fresh	0.093	0.009	0.102	0.907	0.093
Filtered Fresh + Scat.	0.138	0.547	0.685	0.202	0.798
Fresh + Scat. + Abs.	0.764	0.576	1.34	0.57	0.43
As Delivered	0.196	1.284	1.48	0.133	0.867
Filtered 40 min	0.188	0.407	0.595	0.315	0.685
Filtered 1hr 40 min	0.093	0.081	0.174	0.537	0.463
Filtered 18hr	0.085	0.008	0.093	0.909	0.091

Table 5.2: Petzold IOP summary [11]. I'll pull a few cases from here and point out when the asymptotic approximation will work.

CHAPTER VI

MODEL ANALYSIS

6.1   Grid Study

Run many grid sizes with GMRES, using asymptotic solution as initial guess. Compare CPU times and accuracy, assuming largest grid is "true" solution. Determine necessary grid size to achieve reasonable accuracy.

6.2   Asymptotic Convergence

Compare asymptotic solutions to GMRES with reasonable grid size as determined above. Compare CPU time and accuracy. Determine ideal number of scatters to include (number of terms in asymptotic series). Repeat for a few values of scattering coefficient.

6.3   Sensitivity Analysis

Vary parameters and measure average differences in radiance for full grid, as well as average irradance over depth.

       - absorption coefficient

       - scattering coefficient

- VSF

- frond bending coefficient

6.4   Kelp Cultivation Simulation

Run Ole Jacob's model with my new light model, compare:

- irrad over time for several depths

- computation time

- harvestable biomass

CHAPTER VII

CONCLUSION

We present a probabilistic model for the spatial distribution of kelp, and develop a first-principles model for the light field, considering absorption and scattering due to the water and kelp. A full finite difference solution is presented, and an asymptotic approximation based on discrete scattering events is subsequently developed.

Future work:

- Frond bending

- Horizontal kelp ropes (long lines)

- etc.

BIBLIOGRAPHY

[1] N. Anderson. A mathematical model for the growth of giant kelp. *Simulation*, 22(4):97–105, 1974.

[2] O. J. Broch and D. Slagstad. Modelling seasonal growth and composition of the kelp Saccharina latissima. *Journal of Applied Phycology*, 24(4):759–776, Aug. 2012.

[3] M. A. Burgman and V. A. Gerard. A stage-structured, stochastic population model for the giant kelpMacrocystis pyrifera. *Marine Biology*, 105(1):15–23, 1990.

[4] M. F. Colombo-Pallotta, E. Garca-Mendoza, and L. B. Ladah. Photosynthetic Performance, Light Absorption, and Pigment Composition of Macrocystis Pyrifera (laminariales, Phaeophyceae) Blades from Different Depths1. *Journal of Phycology*, 42(6):1225–1234, Dec. 2006.

[5] P. Duarte and J. G. Ferreira. A model for the simulation of macroalgal population dynamics and productivity. *Ecological modelling*, 98(2-3):199–214, 1997.

[6] B. Hamre, . Frette, S. R. Erga, J. J. Stamnes, and K. Stamnes. Parameterization and analysis of the optical absorption and scattering coefficients in a western

Norwegian fjord: a case II water study. *Applied Optics*, 42(6):883, Feb. 2003.

[7] G. A. Jackson. Modelling the growth and harvest yield of the giant kelp Macrocystis pyrifera. *Marine Biology*, 95(4):611–624, 1987.

[8] C. Mobley. *Light and Water: Radiative Transfer in Natural Waters*. Academic Press, 1994.

[9] C. Mobley. Radiative Transfer in the Ocean. In *Encyclopedia of Ocean Sciences*, pages 2321–2330. Elsevier, 2001.

[10] M. Nyman, M. Brown, M. Neushul, and J. A. Keogh. *Macrocystis pyrifera in New Zealand: testing two mathematical models for whole plant growth*, volume 2. Sept. 1990.

[11] T. J. Petzold. Volume Scattering Function for Selected Ocean Waters. Technical report, DTIC Document, 1972.

[12] M. Scheffer, J. Baveco, D. DeAngelis, K. Rose, and E. van Nes. Super-individuals a simple solution for modelling large populations on an individual basis. *Ecological Modelling*, 80:161–170, Mar. 1994.

[13] A. Sokolov, M. Chami, E. Dmitriev, and G. Khomenko. Parameterization of volume scattering function of coastal waters based on the statistical approach. *Optics express*, 18(5):4615–4636, 2010.

[14] P. Wassmann, D. Slagstad, C. W. Riser, and M. Reigstad. Modelling the ecosystem dynamics of the Barents Sea including the marginal ice zone. *Journal of Marine Systems*, 59(1-2):1–24, Jan. 2006.

[15] A. Yoshimori, T. Kono, and H. Iizumi. Mathematical models of population dynamics of the kelp Laminaria religiosa, with emphasis on temperature dependence. *Fisheries Oceanography*, 7(2):136146, 1998.

APPENDICES

APPENDIX A

GRID DETAILS

The width of the spatial grid cells in each dimension are

$$dx = \frac{x_{\max} - x_{\min}}{n_x},$$

$$dy = \frac{y_{\max} - y_{\min}}{n_y},$$

$$dz = \frac{z_{\max} - z_{\min}}{n_z}.$$

Denote the edges as

$$x_i^e = (i-1)dx \text{ for } i = 1, \ldots, n_x$$

$$y_j^e = (j-1)dy \text{ for } j = 1, \ldots, n_y$$

$$z_k^e = (k-1)dz \text{ for } k = 1, \ldots, n_z$$

and the cell centers as

$$x_i = (i-1/2)dx \text{ for } i = 1, \ldots, n_x$$

$$y_j = (j-1/2)dy \text{ for } j = 1, \ldots, n_y$$

$$z_k = (k-1/2)dz \text{ for } k = 1, \ldots, n_z$$

Note that in this convention, there are the same number of edges and cells, and edges precede centers.

Now, we define the azimuthal angle such that

$$\theta_l = (l-1)d\theta.$$

For the sake of periodicity, we need

$$\theta_1 = 0,$$

$$\theta_{n_\theta} = 2\pi - d\theta,$$

which requires

$$d\theta = \frac{2\pi}{n_\theta}.$$

For the polar angle, we similarly let

$$\phi_m = (m-1)d\phi$$

Since the polar azimuthal is not periodic, we also store the endpoint, so

$$\phi_1 = 0,$$

$$\phi_{n_\phi} = \pi.$$

This gives us

$$d\phi = \frac{\pi}{n_\phi - 1}.$$

It is also useful to define the edges between angular grid cells as

$$\theta_l^e = (l-1/2)d\theta, \qquad l = 1,\ldots,n_\theta \tag{A.1}$$

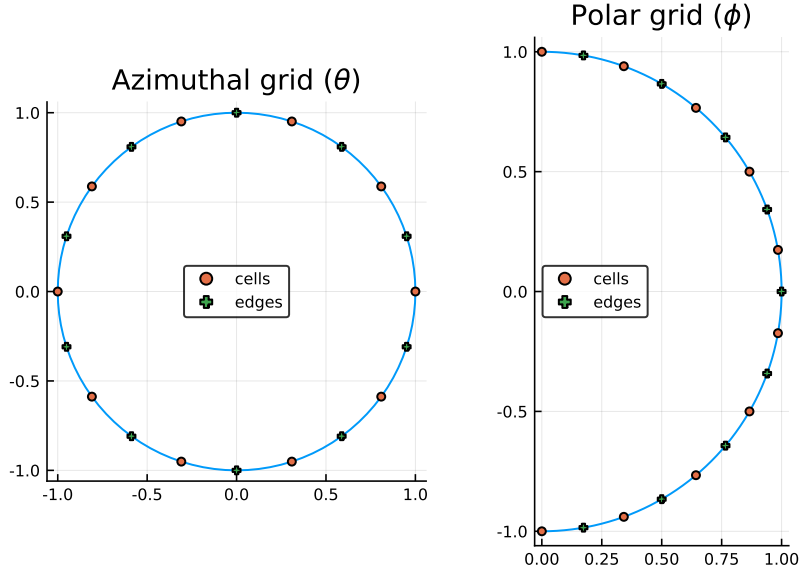$$\phi_m^e = (m-1/2)d\phi, \quad m = 1,\ldots,n_\phi - 1. \tag{A.2}$$

Figure A.1: Angular grid

Note that while θ has its final edge following its final center, this is not the case for ϕ.

The following notation is used.

$$\hat{l}(p) = \mathrm{mod1}(p, n_\theta)$$

$$\hat{m}(p) = \mathrm{ceil}(p/n_\theta) + 1$$

$$\hat{\theta}_p = \theta_{\hat{l}(p)}$$

$$\hat{\phi}_p = \phi_{\hat{m}(p)}$$

Thus, it follows that

$$p = (\hat{m}(p) - 2)\, n_\theta + \hat{l}(p).$$

Accordingly, define

$$\hat{p}(l, m) = (m - 1)n_\theta + l.$$

Further, we refer to the angular grid cell centered at $\boldsymbol{\omega}_p$ as Ω_p, and the solid angle subtended by Ω_p is denoted $|\Omega_p|$. The areas of the grid cells are calculated as follows. Note that there is a temporary abuse of notation in that the same symbols ($d\theta$ and $d\phi$) are being used for infinitesimal differential and for finite grid spacing.

For the poles, we have

$$
\begin{aligned}
|\Omega_1| = |\Omega_{n_\omega}| &= \int_{\Omega_1} d\boldsymbol{\omega} \\
&= \int_0^{2\pi} \int_0^{d\phi/2} \sin\phi \, d\phi \, d\theta \\
&= 2\pi \cos\phi \Big|_{d\phi/2}^0 \\
&= 2\pi(1 - \cos(d\phi/2))
\end{aligned}
$$

And for all other angular grid cells,

$$
\begin{aligned}
|\Omega_p| &= \int_{\Omega_p} d\boldsymbol{\omega} \\
&= \int_{\theta_l^e}^{\theta_{l+1}^e} \int_{\phi_m^e}^{\phi_{m+1}^e} \sin(\phi) \, d\phi \, d\theta \\
&= d\theta \int_{\phi_m^e}^{\phi_{m+1}^e} \sin(\phi) \, d\phi \\
&= d\theta \left(\cos(\phi_m^e) - \cos(\phi_{m+1}^e) \right).
\end{aligned}
$$

APPENDIX B

RAY TRACING ALGORITHM

In order to evaluate a path integral through the previously described grid, it is first necessary to construct a one-dimensional piecewise constant integrand which is discontinuous at unevenly spaced points corresponding to the intersections between the path and edges in the spatial grid.

Consider a grid center $\boldsymbol{p_1} = (p_{1x}, p_{1y}, p_{1z})$ and a corresponding path $\boldsymbol{l}(\boldsymbol{x_1}, \boldsymbol{\omega}, s)$. To find the location of discontinuities in the itegrand, we first calculate the distance from its origin, $\boldsymbol{p_0} = \boldsymbol{x_0}(\boldsymbol{p_1}, \boldsymbol{\omega}) = (p_{0x}, p_{0y}, p_{0z})$ to grid edges in each dimension separately.

Given

$$x_i = p_{0x} + \frac{s_i^x}{\tilde{s}}(p_{1x} - p_{0x}) \tag{B.1}$$

$$y_j = p_{0y} + \frac{s_j^y}{\tilde{s}}(p_{1y} - p_{0y}) \tag{B.2}$$

$$z_k = p_{0z} + \frac{s_k^z}{\tilde{s}}(p_{1z} - p_{0z}) \tag{B.3}$$

we have

$$s_i^x = \tilde{s}\,\frac{x_i - p_{0x}}{p_{1x} - p_{0x}} \tag{B.4}$$

$$s_i^y = \tilde{s}\,\frac{y_i - p_{0y}}{p_{1y} - p_{0y}} \tag{B.5}$$

$$s_i^z = \tilde{s}\,\frac{z_i - p_{0z}}{p_{1z} - p_{0z}} \tag{B.6}$$

$$\tag{B.7}$$

We also keep a record for each dimension specifying whether the ray increases or decreases in the dimension. Let

$$\delta_x = \text{sign}(p_{0x} - p_{1x}) \tag{B.8}$$

$$\delta_y = \text{sign}(p_{0y} - p_{1y}) \tag{B.9}$$

$$\delta_z = \text{sign}(p_{0z} - p_{1z}) \tag{B.10}$$

For convenience, we also store a closely related quantity, σ with a value 1 for increasing rays and 0 for decreasing rays in each dimension

$$\sigma_x = (\delta_x + 1)/2 \tag{B.11}$$

$$\sigma_y = (\delta_y + 1)/2 \tag{B.12}$$

$$\sigma_z = (\delta_z + 1)/2 \tag{B.13}$$

For this algorithm, we keep two sets of indices. (i, j, k) indexes the grid cell, and will be used for extracting physical quantities from each cell along the path. Meanwhile, (i^e, j^e, k^e) will index the edges between grid cells, beginning after the first cell. i.e., $i^e = 1$ refers not to the plane $x = x_{\text{min}}$, but to $x = x_{\text{min}} + dx$.

62

Let (i_0, j_0, k_0) be the indices of the grid cell containing $\boldsymbol{p_0}$.

That is,

$$i_0 = \text{ceil}\left(\frac{p_{0x} - x_{\min}}{dx}\right) \tag{B.14}$$

$$j_0 = \text{ceil}\left(\frac{p_{0y} - y_{\min}}{dy}\right) \tag{B.15}$$

$$k_0 = \text{ceil}\left(\frac{p_{0z} - z_{\min}}{dz}\right) \tag{B.16}$$

Then,

$$i_0^e = i_0 + \sigma_x \tag{B.17}$$

$$j_0^e = j_0 + \sigma_y \tag{B.18}$$

$$k_0^e = k_0 + \sigma_z \tag{B.19}$$

Now, we calculate the distance from p_0 along the path to edges in each dimension.

$$s_i^x = \hat{s}\frac{x_i^e - p_{0x}}{p_{1x} - p_{0x}} \tag{B.20}$$

$$s_j^y = \hat{s}\frac{y_j^e - p_{0y}}{p_{1y} - p_{0y}} \tag{B.21}$$

$$s_k^z = \hat{s}\frac{z_k^e - p_{0z}}{p_{1z} - p_{0z}} \tag{B.22}$$

For each grid cell, we check the path lengths required to cross the next x, y, and z edge-planes. Then, we move to the next grid cell in that dimension. That is,

* We also track s, the path length.

Consider i, j, k fixed (denoting the current grid cell).

$$d = \mathrm{argmin}_{x,y,z} \left\{ s_i^x - s, s_j^y - s, s_k^z \right\} \tag{B.23}$$

* This doesn't quite make sense yet.

$$\begin{cases} i = i + \delta_x, & \text{if } d = x \\ j = j + \delta_y, & \text{if } d = y \\ z = k + \delta_z, & \text{if } d = z \end{cases} \tag{B.24}$$

and

$$\begin{cases} i^e = i^e + \delta_x, & \text{if } d = x \\ j^e = j^e + \delta_y, & \text{if } d = y \\ z^e = k^e + \delta_z, & \text{if } d = z \end{cases} \tag{B.25}$$

Then, move to the adjacent grid cell in the dimension which requires the shortest step to reach an edge. Save ds of the path through this cell. Also save abs. coef. and source.